The Generation of Hydroxyl Radicals by Hydrogen Peroxide Decomposition on FeOCl/SBA-15 Catalysts for Phenol Degradation

Xue-jing Yang, Peng-fei Tian, Xiao-man Zhang, Xin Yu, Ting Wu, Jing Xu, and Yi-fan Han
Dept. of Chemical Engineering, State Key Laboratory of Chemical Engineering, East China University of Science and Technology, Shanghai 200237, China

DOI 10.1002/aic.14625
Published online September 20, 2014 in Wiley Online Library (wileyonlinelibrary.com)

Iron oxychloride (FeOCl) supported on mesoporous silica (SBA-15), as a Fenton-like solid catalyst for phenol degradation, showed supreme activity for production of hydroxyl radical (HO·) by H_2O_2 decomposition, and the generation capacity was comparable to the conventional Fenton reagent ($Fe^{2+}+H_2O_2$). The structure of FeOCl was characterized with spectroscopies. The generation of HO· species during the reaction was detected using 5,5-dimethyl-1-pyrroline N-oxide trapped electron paramagnetic resonance. Furthermore, the kinetics in detail was driven for the creation and diffusion of HO· by H_2O_2 decomposition over FeOCl, which follows a first-order rate through a two-step reaction. With the combination of the catalyst structure and kinetic parameters, the plausible mechanism for H_2O_2 decomposition during the oxidative degradation of phenol was rationalized. As a Fenton-like solid catalyst, FeOCl/SBA-15 is a promising alternative for the removal of low-level organic contaminates from water. © 2014 American Institute of Chemical Engineers *AIChE J*, 61: 166–176, 2015

Keywords: iron oxychloride, hydroxyl radicals, hydrogen peroxide, phenol degradation, Fenton-like catalyst, kinetics

Introduction

The increasing worldwide contamination of surface water is a crucial environmental problems.[1] In particular, the treatment of refractory (or nonbiodegradable) organic compounds (ROC) with extremely low concentration (ppm level) is a great challenge in the production of clean water because of its high operational cost and potential secondary pollution using conventional methods.[2] As the enforcement of restrict law on the quality of freshwater, the development of novel approach for purifying the contaminated water is highly desired.

Fenton process is one of the most promising techniques for ROC treatment, due to the repaid generation of hydroxyl radicals (HO·), which has proven powerful oxidants.[3–5] HO· can completely oxidize ROC into CO_2 and H_2O without light, heat, and electricity. The conventional Fenton reagent usually consists of iron ion (Fe^{2+} or Fe^{3+}) and H_2O_2, being applied in water industry nearly a half century ago.[6] However, there are still several formidable drawbacks for this process. For instance, (1) the working pH range is too narrow (pH:2.5–3.5); (2)the continuous addition of Fe^{2+} during reaction due to the loss of Fe^{2+} by deposition increases the operational cost; and (3) the accumulation of iron-containing sludge leads to the secondary pollution.

Therefore, to overcome the aforementioned drawbacks, the advanced oxidation system with the combination of various iron-free Fenton-like solid catalysts has been developed to substitute for Fe^{2+},[7–9] such as Cu,[10–12] Mn,[13,14] Co,[15] Ce,[16] and Au.[17–19] The output of sludge is expected to be remarkably reduced. However, the performances of those Fe-free catalysts are still not comparable to iron-containing system. Natural or synthetic iron minerals have also been widely studied for this reaction system, such as hematite,[20] goethite,[21] ferrihydrite,[22] and magnetite[23]. Nevertheless, the rate of HO· generation over those Fe-based Fenton-like catalysts is still lower than that for Fe^{2+}in aqueous solution by 2–3 magnitudes. The primary reason is possible due to the relatively low surface area of those bulk materials. Consequently, porous support materials with high surface area, such as carbon,[24,25] polymer membrane,[26,27] silica,[28,29] clay,[30] or zeolite,[31,32] have been used to increase the dispersion of iron-containing active sites. A new challenge is arisen on how to stabilize Fe atoms under reaction conditions, because the remarkable leaching of iron cannot be avoided by all approaches in those systems. Up to now, the development of excellent solid Fenton-like catalysts as well as facilitation on preparation is still of great concern.

With the assistance of femtosecond laser, Kiwi et al. found that the linearship configuration of Fe species ([Fe—O—Fe]) may contribute to the generation of HO·.[27,33] This structure was abundant in layered iron materials such as FeOCl, which is a functional material with a self-stacked layer and ever used as cathode.[34] The layered FeOCl can accommodate the intercalated electron-donor molecules

Correspondence concerning this article should be addressed to Yi-fan Han at yifanhan@ecust.edu.cn.

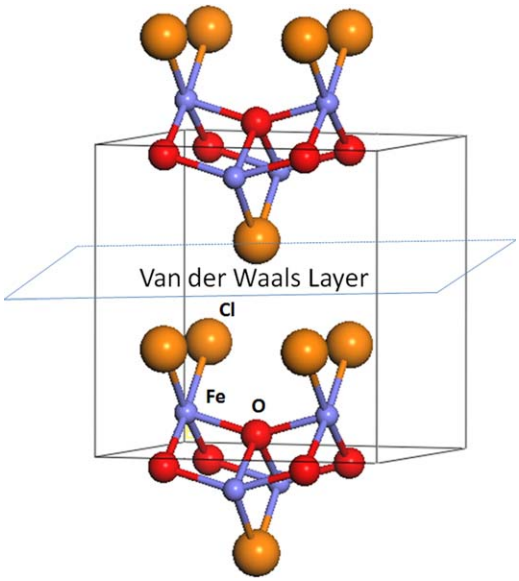

Scheme 1. Crystalline structure of FeOCl.

[Color figure can be viewed in the online issue, which is available at wileyonlinelibrary.com.]

(Scheme 1). Within the so-called "Van de Waals layer," charge transfer between organic molecules and ferric ion can occur readily (Eq. 1).[35] We assume that the ferrous ion may trigger the Fenton reaction (Eq. 2). The superior capability of FeOCl for the generation of HO· was demonstrated by a molecular probe method[36]

$$FeOCl + nI \leftrightarrow Fe_{1-n}^{III}Fe_n^{II}OCl + nI^+ \quad (1)$$

$$Fe^{II} + H_2O_2 \rightarrow Fe^{III} + HO\cdot + OH^- \quad (2)$$

We recently have reported that the pure FeOCl catalyst outperformed the traditional Fenton reagent on yielding HO· by H_2O_2 decomposition. The generation rate of HO· over FeOCl was higher by about 3–4 orders of magnitudes than other Fenton-like systems.[36] However, the preparation process of this material is too complex to be applied in practice. To improve the efficiency of FeOCl, in this study, we disperse FeOCl on a mesoporous silica (SBA-15) by partial decomposition of $FeCl_3{\cdot}6H_2O$ via a modified melt-infiltrate method.[37,38] The origin of active sites and reaction mechanism are systematically rationalized through a model reaction in the case of phenol degradation and H_2O_2 decomposition. Phenol is usually regarded as an important intermediate for the degradation of aromatic hydrocarbons,[39] also an ideal model persistent organic compounds that is hardly remediated through biodegradation.

The FeOCl/SBA-15 catalyst as well as other reference Fe/SBA-15 catalysts are characterized by multitechniques, such as X-ray diffraction (XRD), scanning electron microscopy (SEM), infrared (IR), laser Raman spectroscopy (LRS), and UV-vis spectroscopies. Moreover, to identify HO·, 5,5-dimethyl-1-pyrroline *N*-oxide (DMPO) trapped electron paramagnetic resonance (EPR) was performed. Conversely, the detailed kinetics for the catalytic decomposition of H_2O_2 is performed. With considering the kinetic modeling of H_2O_2 decomposition, a plausible mechanism was finally proposed including the generation of HO·. To the best of our knowledge, herein, for the first time the dynamic process of H_2O_2 decomposition over FeOCl-based catalyst was illustrated. This study may point out a great perspective for the design of new solid Fenton-like catalysts as well as the catalysts based on FeOCl, which is potentially applied for purifying water.

Experimental Section

Catalyst preparation

SBA-15 was synthesized by a reported method using triblock copolymer Pluronic 123 (P123, Sigma Aldrich) as a template and tetraethoxysilane (TEOS, Lingfeng Chemical Reagent Co., China) as silica source.[40] The template was first dissolved into hydrochloric acid (13 wt %). Silica source was then dropped to the light blue emulsion at 313 K with a stirring rate of 450 rmp for 24 h. The obtained gel was then hydrothermally treated in a sealed polypropylene jar at 373 K for 24 h. After filtration and washing with MilliQ water, the precursor was dried at 353 K overnight. Finally, the sample was calcined at 823 K for 6 h. It is noted that by blank tests (H_2O_2 500 mg/L or phenol 100 mg/L) all supports were evidenced to be inert to H_2O_2 decomposition and phenol adsorption under reaction conditions.

A modified melt infiltration method, which is also known as a solvent-free method, was used for the preparation of catalysts.[41] $FeCl_3{\cdot}6H_2O$ (AR, from Sinoreagent, China) was selected as iron source. Corresponding to a loading amount of 10 wt % Fe, $FeCl_3{\cdot}6H_2O$, and SBA-15 were first mechanically mixed in an agate mortar for 10 min under ambient conditions till the powder became uniformly lemon yellow. Then, the precursor was transferred to a sealed glass vessel for infiltration by 24 h at 353 K. Finally, the obtained powder was calcined in an air flow (20 mL/min) at 623 K for 30 min until its color became purple. The sample was denoted as Fe/SBA-15-MF.

Fe/SBA-15-CC was prepared with a cocondensation method reported by Lázár et al.[42] $FeCl_3{\cdot}6H_2O$ and TEOS were first self-assembled under acidic conditions with the P123 template. Then, the sample was aged at 383 K for 24 h after the adjustment of pH to 3.5 by ammonia. The solids were filtered and washed by Milli Q water till it became neutral. After dried at room temperature overnight, the sample was sintered in air at 823 K for 5 h.

Fe/SBA-15-IM was synthesized through a wet impregnation method.[43] $FeCl_3$ solution of 2 mL (11.9 M) was dropped into 0.3 g SBA-15 powder under continuously stirring. The precursor was dried overnight at 313 K, and then calcined at 573 K in air for 30 min with a ramping rate of 10 K/min.

A chemical-vapor-transport technique was adopted for the synthesis of FeOCl.[44] α-Fe_2O_3 (GR, Aladdin Reagent, China) was mixed with anhydrous $FeCl_3$ (CP, Sinoreagent, China) with a molar ratio of 1:1.3. The obtained powder was sealed in a glass container. The sealed container which was transferred to a muffle furnace was then heated to 653 K for 40 h. After rinsing with anhydrous acetone for the removal of the excess $FeCl_3$ and vacuum dried at 313 K overnight, dark purple powders were obtained finally.$FeSO_4{\cdot}7H_2O$ (AR, Sinoreagent, China) was used as the ferrous source of homogenous Fenton reagent.

The modeling of the kinetic data and the reaction prediction were undertaken with the assistance of DynaFit (4. 05. 087 version).[45]

Characterization

XRD. XRD patterns were obtained with a Riguku D/max 2550 diffractometer using Cu Kα radiation ($\lambda = 1.540589$ Å), which was operated at the accelerated voltage of 40 kV

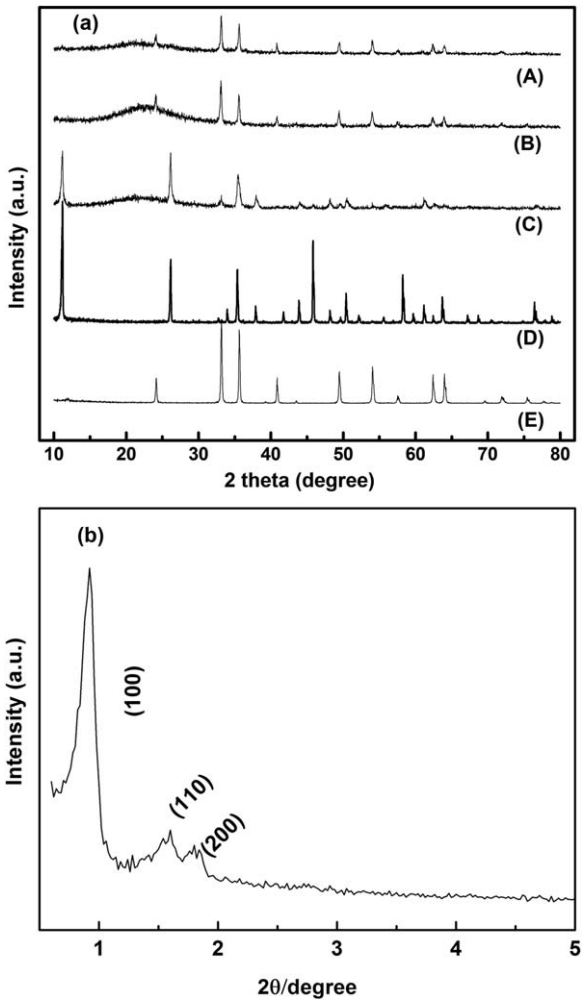

Figure 1. XRD patterns of as-prepared catalysts (a): Fe/SBA-15-IM (A), Fe/SBA-15-CC (B), Fe/SBA-15-MF(C), FeOCl (D), α-Fe_2O_3 (E) and (b) low-angle XRD of the pure SBA-15.

and the detector current of 100 mA. The diffraction patterns were recorded in the Bragg angle (2θ) range of 10–80°with a step size of 0.02°. Phase identification was performed with referring the standard JCPDS cards from ICCD.

LRS. LRS was recorded using a LabRam HR, Horiba JY Raman spectroscopy. It consists of a spectrograph of 800 mm in focal length, a kinematics grating of 1800 g/mm and an air-cooled CCD detector (1024 × 256 pixels, 26 μm in size). The powder sample was attached and flattened over a glass slide. The spectrum was excited by a 632.817 nm He-Ne laser with the power fixed to 20 mW. The beam was focused on the sample by a ×50 lens (Olympus) with the focal distance of 26.5 mm to give a spot size of 2 μm. The final resolution of about 1.5 $cm^{-1}$was obtained. The confocal hole was set to 200 μm to all tests. The attenuator was used for avoiding the signal overflow and the sample degradation. The exposure time was set to 100 s for each spectrum. The single crystal silicon was used for position correction.

IR. Two modes IR spectroscopy were performed using a Perkin Elmer Spectrum 100 Fourier Transform Infrared (FTIR) spectroscopy with dual detectors. For the transmittance IR spectroscopy, the sample pellets with the catalyst powder dispersed in KBr (SP, Sinoreagent, China) matrix were scanned in a wavelength range 1400–400 cm^{-1}. The data were collected by a DTGS detector, while the Attenuated Total Reflection (ATR)-FTIR spectroscopy in the range 4000–1400 cm^{-1} were recorded using a UATR accessory and a MCT (Hg-Cd-Te) detector. The catalysts were directly attached to the sample panel without any pretreatment. A resolution of 4 cm^{-1} was performed for all experiments.

UV-vis. Diffuse reflectance UV-vis spectra were collected using a Varian Cary 500 spectrophotometer equipped with a diffuse reflectance accessory (Praying Mantis, Harrick) in the range of 200–800 nm. The powdery sample was loaded into a quartz cell. All tests were carried out in ambient conditions with referring to $BaSO_4$ crystal.

SEM. The measurements of SEM images were carried out using a FEI NOVA NanoSEM 450 SEM, which was operated at the accelerating voltage of 15 kV and the detector current of 10 mA. The collection was taken at high vaccum mode (1×10^{-3} mbar) with a beam spot of 3 μm.

EPR. DMPO trapped EPR spectroscopy was obtained for various supported catalysts. Meanwhile, the trapped signals from FeOCl, α-$Fe_2O_3$and $FeSO_4{\cdot}7H_2O$ were compared under the same conditions. We used a Bruke EMX-8/2.7C spectrometer, which was operated at X-field with a center field at 3511.520G and a sweep width of 200G. The microwave frequency is 9.873 GHz and the power is 2.016 mW. Sweep time of the signal channel is 41.9 s with a 3.56×10^4 gain

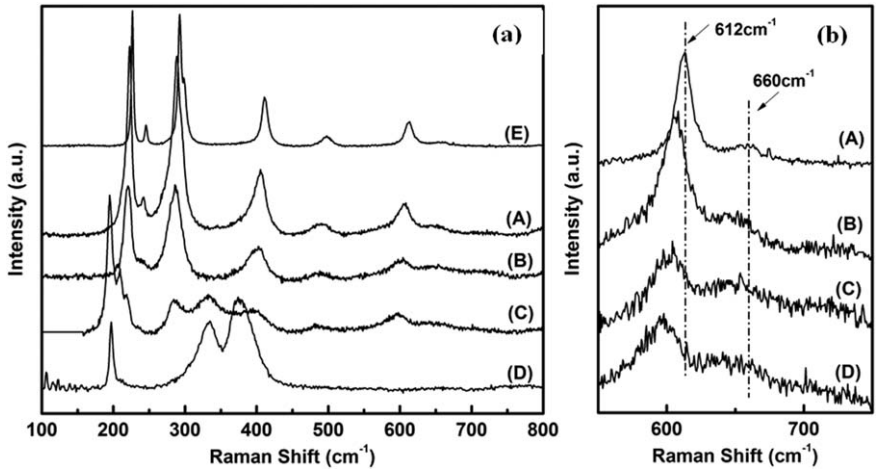

Figure 2. Raman spectra in the range of 100–800 cm^{-1}(a)and 550–750 cm^{-1} (b) of as-prepared catalysts: Fe/SBA-15-IM (A), Fe/SBA-15-CC (B), Fe/SBA-15-MF (C), FeOCl(D),α-Fe_2O_3 (E).

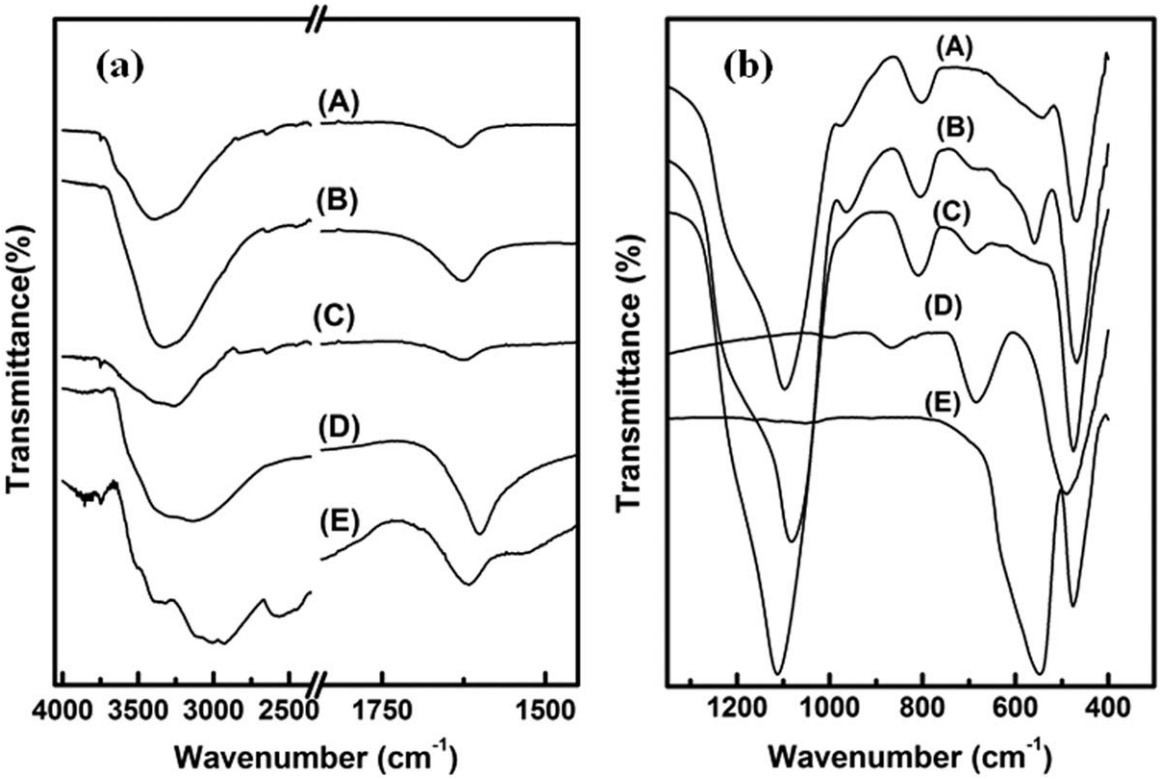

Figure 3. ATR-FTIR (a) and Transmittance FTIR (b) spectra of as-prepared catalysts: Fe/SBA-15-IM (A), Fe/SBA-15-CC (B), Fe/SBA-15-MF(C), FeOCl (D), α-Fe_2O_3 (E).

at the receiver. Before each experiment, catalyst with a certain weight (equal to Fe 0.35 mM) was added to 200 mL aqueous solution containing 500 mg/L (14.71 mM) H_2O_2; the pH value was adjusted to 4.5 using 0.01 M HNO_3 solution. After stirring for 2 min, 1 mL aliquots was ejected to 1 mL DMPO (100 mg/L, ESR grand, Sigma Aldrich) immediately. The obtained solution was transferred into a 100 μL capillary tube, which was then fixed in the resonant cavity of the spectrometer. The whole experiment was performed at room temperature.

N2 Adsorption- Desorption Isotherm. N_2 adsorption-desorption isotherms were collected using ASAP 2010 (Micromeritics) at 77 K. Prior to the measurement, all samples were degassed at 303 K until a stable vacuum of about 5 m Torr was reached. The pore distribution curves were calculated from the adsorption branch using the Density Functional Theory (DFT) method. The specific surface area was assessed using the BET method from adsorption data in a relative pressure range from 0.06 to 0.35. The conversion factor between the volume of gas and liquid adsorbate is 0.0015468 for N_2 at 77 K, being expressed in cm^3/g and cm^3 STP/g, respectively.

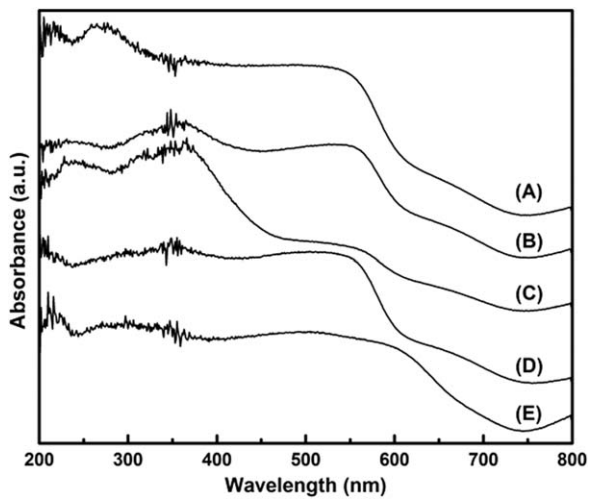

Figure 4. Diffuse reflectance UV-vis spectra of the synthetic catalysts: Fe/SBA-15-IM (A), Fe/SBA-15-CC (B), Fe/SBA-15-MF(C), FeOCl (D), α-Fe_2O_3 (E).

Activity measurement

The solution with a mixture of phenol (1000 mg/L) and H_2O_2(5000 mg/L) was prepared with MilliQ water (18.25MΩ) while the pH value was adjusted with 0.1 mol/LHNO_3. For each experiment, 100 mL reaction solution was poured into a thermo-constant batch reactor. Aliquots of 2 mL for analysis were taken at interval of 2 or 5 min, following with the filtration by a 0.22 μm nylon membrane. The concentration of phenol was measured using a High Performance Liquid Chromotograph (HPLC) (Perkin Elmer Flexar) that was equipped with a Spheri-5 C18 column and UV detector (wavelength 275 nm).[39] The variation of H_2O_2 concentration during reaction was analyzed colorimetrically using a UV-vis spectrophotometer after complexation with a $TiOSO_4/H_2SO_4$ reagent.[46] The pH of the solution was monitored by a pH meter (Leici PHS-3D, China), which was kept within ±0.1 pH unit.

The leaching of iron was introductive coupled plasma mass spectrometry (ICP-MS; Perkin Elmer, NexION 300).

Results and Discussion

Catalyst structure

XRD patterns of the as-prepared catalysts were shown in Figure 1a. With referring to JCPDS cards (No.33–0664,

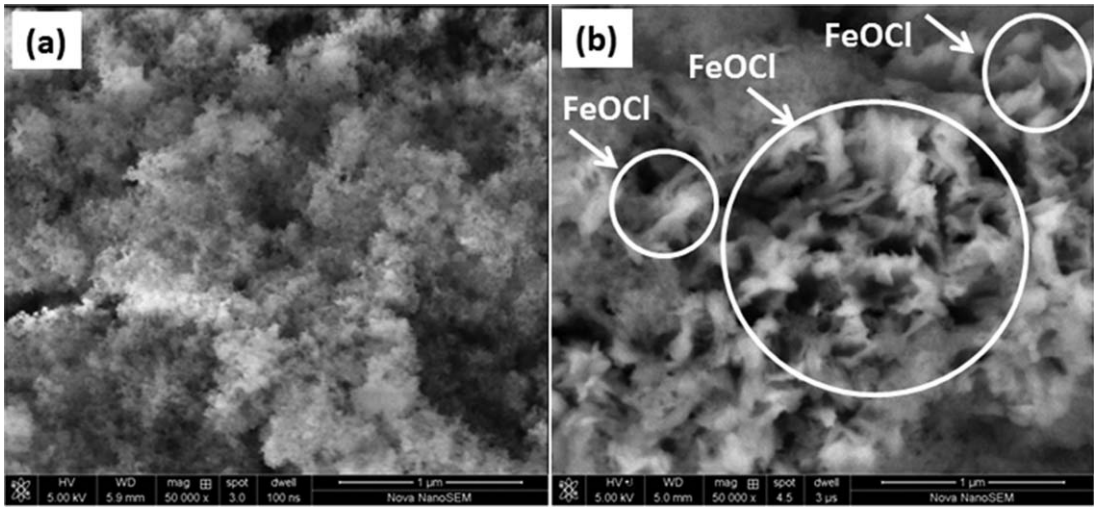

Figure 5. SEM images of SBA-15 (a) and Fe/SBA-15-MF (b).

39–0612, 72–0169, and 73–2229), crystalline hematite (α-Fe_2O_3) was embedded into the catalyst prepared by the impregnation method (Fe/SBA-15-IM, pattern A in Figure 1) and the cocondensation method (Fe/SBA-15-CC, pattern B in Figure 1a, respectively[29,43]; meanwhile, FeOCl crystalline was detectable in Fe/SBA-15-MF(pattern C in Figure 1a). The highest intensity at the peak (010) ($2\theta = 11.67$) indicated a remarkable orientation effect along the *b* axis. The diffraction patterns of unsupported FeOCl (pattern D in Figure 1a) and hematite (Spectrum E and in Figure 1a) were also presented as references. The crystalline degree for pure FeOCl was significantly higher than the supported catalysts. Conversely, the low-angle XRD pattern of the unloaded SBA-15 was displayed in Figure 2b as well. It is a typical mesoporous materials with ordered pore structure.

Raman spectra show the A_{1g} mode (222, 496 cm^{-1}) and E_g mode (242, 291, 408, and 612 cm^{-1}) of the Fe—O stretching vibration for unsupported hematite powder (Spectrum E in Figure 2a).[47] Additionally, the longitudinal optical (LO) mode at 660 cm^{-1} can be observed for all catalysts, due to the high frequency limit for the lattice Fe—O vibration and the disorder (bending or libration vibration) generating from adsorbed hydroxyls (or water). The intensity ratio of the band at 660 cm^{-1} *vs*. the E_g band at 612 cm^{-1} was supposed to be related to the crystal size and the crystalline degree of hematite.[48] Tanking a close to the LRS in the range 550–750 cm^{-1} (Figure 2b), we found that the E_g band was weakened while the LO band was enhanced significantly; this indicated that the nanosized hematite may be formed in supported catalysts. The size of hematite for Fe/SBA-15-IM (Spectrum A in Figure 2a) could be larger than that of Fe/SBA-15-CC. Meanwhile, the A_{1g} peak at 219 cm^{-1} of unsupported hematite shifted down to 211 cm^{-1} after supporting (Spectrum B and E in Figure 2a). This phenomenon as well as the broadening of the peak also indicates a decrease in crystal size.[49]

Since the Raman spectroscopy of FeOCl has never been reported, the assignment of the bands for FeOCl is referred to those for γ-FeOOH (Lepidocrocite) because of their similarity on the structure. FeOCl was identified with a well-known self-stacked layer up-taking the intercalated molecules, or to say, "Van de Waals layer" (Scheme 1). The strong band at 200 cm^{-1} may be attributed to the Fe—Cl bond. The broad scatterings at 330 and 390 cm^{-1} were usually observed for the compounds with the Fe—OH bond,[50] which is not unusual for the layered structure of

Table 1. Initial Reaction Rates for Phenol Degradation over Various Fe/SBA-15 Catalysts

Catalyst	Fe Loading (%)	Surface Area (m^2/g)	Activity		$r_{0,phenol}$ ($g_{phenol}/(g_{catal} \times min)$)
			τ (min)	Phenol conv. (%)	
Fe/SBA-15-MF	10.0	633	5	93.3	0.093
			15	100.0	
			90	100.0	
			240	100	
Fe/SBA-15-IM	10.0	572	5	8.9	8.9×10^{-3}
			15	33.5	
			90	60.9	
			240	91.0	
Fe/SBA-15-CC	10.0	602	5	2.7	2.7×10^{-3}
			15	8.6	
			90	23.1	
			240	45.3	
SBA-15	–	679	N.A.	N.A.	N.A.

(a) Initial rate in TOF.
(b) Reaction conditions: pH = 4.5, 313 K, $[phenol]_0$: 100 mg/L (1.06 mM), $[H_2O_2]_0$: 500 mg/L(14.67 mM), catalyst amount 200 mg/L.

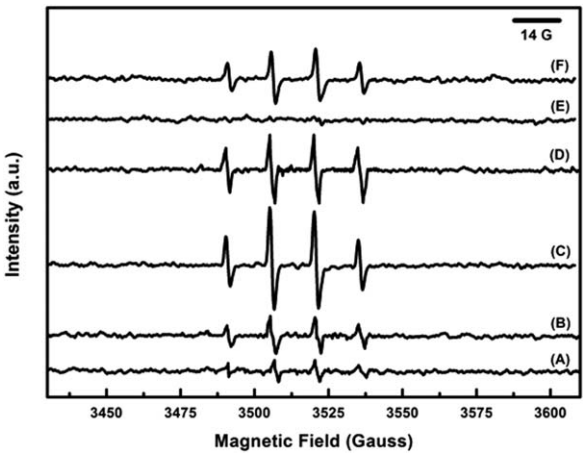

Figure 6. DMPO-trapped EPR spectra of HO·generated from the different catalysts: Fe/SBA-15-IM (A), Fe/SBA-15-CC (B), Fe/SBA-15-MF(C), FeOCl (D), α-Fe_2O_3 (E), Fe^{2+} (F).

FeOOH.[51–53] With referring to the LRS of Fe/SBA-15-MF (Spectrum C in Figure 2a), the catalyst is assumed to consist of FeOCl crystalline and nano hematite.

IR spectroscopy is considered as a powerful tool for the characterization of iron oxide.[54] The vibration modes of A_{2u}/E_u at 545 cm^{-1} and E_u mode at 480 $cm^{-1}$are usually observed for crystalline hematite, which was also detected in this study (Spectrum E in Figure 3). The E_u band of Fe—O has proven to be greatly dependent on the crystallinity, the size, and the shape of hematite.[55] The red shift of this peak indicates a decrease in the crystalline degree. Meanwhile, the sharp evolution occurred when this vibration was weakened. For instance, the E_u band for Fe/SBA-15-IM at about 468 cm^{-1} (480 cm^{-1} for unsupported hematite) indicates that the particle is flattened along the *c* axis, and a plate-like morphology might be obtained.[55,56] The peak at about 690 cm^{-1} was an indicative of poorly crystalline iron oxide or defective hematite.[57] Therefore, the number of defect sites for Fe/SBA-15-CC (Spectrum B in Figure 3) is probably higher than that for Fe/SBA-15-IM (Spectrum A in Figure 3). The structural disorder may also occur to Fe/SBA-15-MF (Spectrum C in Figure 3). Choy et al.[58] has assigned the band at 480 cm^{-1} to the stretching vibration of Fe—O. To reduce the water impact on KBr matrix, the ATR-FTIR test was carried out for determining the vibrations of different hydroxyl groups. The stretching vibration in the range of 3700–3000 cm^{-1}can be assigned to hydroxyl group (—OH), meanwhile the bending vibration of O—H on iron oxide was observed at about 900 cm^{-1}(δ_{-OH}) and 790 cm^{-1}(γ_{-OH}), respectively. The intensive peaks at about 1600 cm^{-1} (δ_{H-OH}) and 1100 cm^{-1}(ν_{Si-O}) are related to the adsorbed water on the silica surface. Compared to the other two supported catalysts, the stretching of —OH on Fe/SBA-15-MF shifted down to 3240 cm^{-1} (Fe/SBA-15-CC, 3360 cm^{-1}; Fe/SBA-15-IM, 3403 cm^{-1}) while the bending vibration also intensely located at 810 cm^{-1}. This fact indicates a relatively weakly bonded OH group in catalysts.[54]

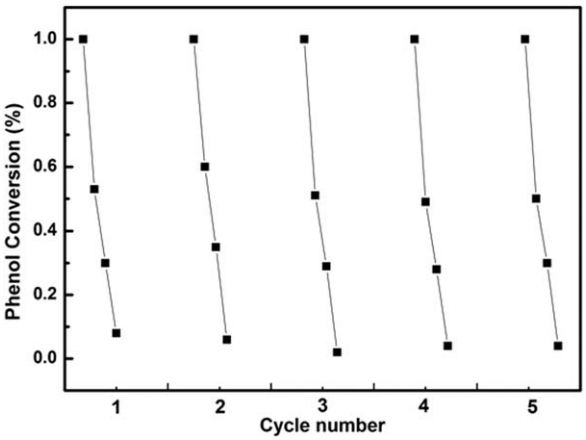

Figure 7. The stability test of Fe/SBA-15-MF.

The electronic properties of iron species were determined using the diffuse reflectance UV-vis spectroscopy. The absorption at 270–280 nm is related to the isolated octahedral Fe^{III} species (Spectrum A in Figure 4). Meanwhile, the broad peak at about 230 nm is a straight forward evidence for the existence of isolated Fe^{III} at tetrahedral coordination sites.[59,60] Small Fe_xO_y clusters or oligomers also existed in Fe/SBA-15-CC and Fe/SBA-15-MF, as identified by the $^6A_1 \rightarrow {}^4E$ energy transition at 300–400 nm (Spectra B and C in Figure 4).[61] The absorption bands at above 400 nm may be caused by relatively larger hematite particles or Fe_2O_3-like clusters. Therefore, the crystalline hematite clearly exists in Fe/SBA-15-IM and Fe/SBA-15-CC as well as the amorphous iron species in different coordination environments. The broad band at above 600 nm was also considered as the transition of $^6A_1 \rightarrow {}^4T_2$ of γ-FeOOH.[62] As for the case of Fe/SBA-15-MF (Spectrum C in Figure 4), the overlap of this peak and the absorption at about 450 nm demonstrates the coexistence of crystalline FeOCl and nanosized hematite.

SEM images (Figure 5) revealed that after the loading of iron, a flat-like material was closely bonded on the surface of SBA-15. We assumed that FeOCl was existing as nanocrystals. The origin of the reactivity may be from the substance (FeOCl) itself or the interaction between FeOCl and SiO_2.

Catalytic performance

The performances of all catalysts were examined in the degradation of phenol, which is a model reaction generally used for the evaluation of the performances of solid Fenton catalysts, because phenol is considered to be an intermediate in the oxidation pathway of higher molecular weight aromatic hydrocarbons.[39] The activity measurement was carried out at the initial pH = 4.5 and 313 K with a catalyst amount of 200 mg/L if without special emphasis. The total transformation of phenol was achieved over Fe/SBA-15-MF within 15 min. However, the final conversion over Fe/SBA-15-CC and Fe/SBA-15-IM was 91.0% and 45.3% within 240 min, respectively. The initial reaction rate of phenol oxidation was calculated by Eq. 3.[39,63,64] As listed in Table 1, the initial rate over Fe/SBA-15-MF was about 10 times higher than that of Fe/SBA-15-CC and Fe/SBA-15-IM

$$-r_{0,\text{phenol}} = \frac{(d[\text{phenol}]/dt)_0}{[\text{catal.}]} \tag{3}$$

HO· generation

It has been evidenced that in the solid Fenton-like systems the decomposition of H_2O_2 was initially controlled by the redox of $Fe^{2+} \leftrightarrow Fe^{3+}$ on the catalyst surfaces. The HO·

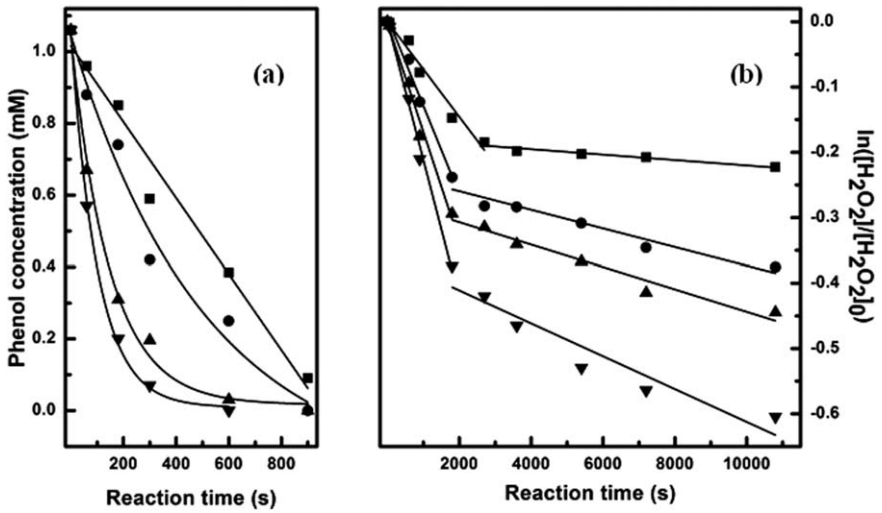

Figure 8. Degradation of phenol (a)and decomposition of H_2O_2 (b) under various loading amount of catalysts:10 mg/L (■); 75 mg/L (•); 100 mg/L (▲); 200 mg/L (▼).

Reaction condition: 313 K, pH = 4.5, $[phenol]_0 = 1.06$ mM, $[H_2O_2]_0 = 14.71$ mM.

consequently generated is responsible for the degradation of phenol,[65] being dependent on active sites on the catalysts. In this study, DMPO-trapped EPR was used for the determination of HO· produced by the decomposition of H_2O_2 over pure and supported FeOCl catalysts (Fe/SBA-15-MF), respectively. In the meantime, HO· generated by a conventional Fenton catalyst, $FeSO_4{\cdot}7H_2O$, was also measured for comparison. EPR signal of the DMPO-HO· adduct demonstrated the generation of HO· for all catalytic systems (Figure 6). Due to the hyperfine interaction between the electron spin of HO· and the orbit spin of nitrogen atom in DMPO, the EPR signal was split into four single lines, with a spacing of 14 G in magnetic field. The g factor of each line is 2.0198, 2.0112, 2.0027, and 1.9941, respectively, with an intensity ratio of 1:2:2:1. Since the sample tubes were identical in the resonant cavity, the volume of solution containing DMPO adducts and the concentration of DMPO are close for three cases. Since the lineshape of the DMPO adduct was also of the same mode, the intensity of the EPR signal reflects the HO·concentration for each catalyst.[66]

Obviously, the amount of HO· generated from Fe/SBA-15-MF (curve C in Figure 6) is the large stone among all the cases, while the signal from unsupported FeOCl was also evidenced (curve E in Figure 6). The excellent generation capacity of HO· over unsopported FeOCl has been already demonstrated in a previous study.[36] The FeOCl species dispersed on Fe/SBA-15-MF were the primary active sites for H_2O_2 decomposition and the subsequent phenol degradation. In particular, the amount of HO· generated from Fe/SBA-15-MFwas close to that from the conventional Fenton agent with the same Fe weight (curve F in Figure 6).Thus, we can conclude that the generation of HO· directly led to the degradation of phenol over all three Fe/SiO_2catalysts. The differences in phenol degradation resulted from the productivity of HO· over each catalyst. Therefore, the kinetics for the creation of HO· by H_2O_2 decomposition over solid Fenton-like catalysts is very important for either understanding the mechanism or reactor design.

Catalyst stability

Prior to the kinetic measurement, the stability of active species in acidic solutions is investigated. The reaction rate for phenol degradation remained unchanged after five cycles (Figure 7). In addition, as analyzed by ICP-MS, the maximum Fe content in the residual solutions was 10 ppb (μg/L), corresponding to about 0.05 wt % of the total Fe loading amount. Therefore, the influence of homogenous catalysis resulting from Fe^{2+} can be safely ruled out.

Kinetics of H_2O_2 decomposition over Fe/SBA-15-MF

In accordance with the "microfluid" theory proposed by Levenspiel,[67] the catalyst should be continuously stirred at 700 rpm to assure the complete mixing. The initial concentration of phenol and H_2O_2 was 100 mg/L and 500 mg/L, respectively. Before the measurement of the catalytic activity, blank test with Fe/SBA-15-MF of 200 mg/L was dosed into the phenol solution (100 mg/L) without the addition of H_2O_2. Within the first 900 s, the reduction of phenol concentration was less than 10%. Thus, we can conclude that the adsorption effect of the catalyst is negligible. With the variation of the loading amounts of catalysts, phenol and H_2O_2 were decomposed simultaneously at 313 K and pH = 4.5, while phenol of 100 mg/L totally degraded over 200 mg/L Fe/SBA-15-MF within 7 min (Figure 8). The decay rates for

Table 2. Rate-Constants of H_2O_2 Decay over Fe/SBA-15-MF

Catalyst loading amount (mg/L)	Step 1		Step 2	
	k_{obs} (s^{-1})	r^2	k_{obs} (s^{-1})	r^2
10	$(7.29 \pm 0.59) \times 10^{-5}$	0.97	$(4.15 \pm 0.63) \times 10^{-6}$	0.91
75	$(13.51 \pm 0.77) \times 10^{-5}$	0.99	$(14.23 \pm 1.82) \times 10^{-6}$	0.95
100	$(16.74 \pm 1.06) \times 10^{-5}$	0.99	$(17.10 \pm 1.75) \times 10^{-6}$	0.93
200	$(21.17 \pm 9.11) \times 10^{-5}$	0.98	$(25.17 \pm 4.04) \times 10^{-5}$	0.88

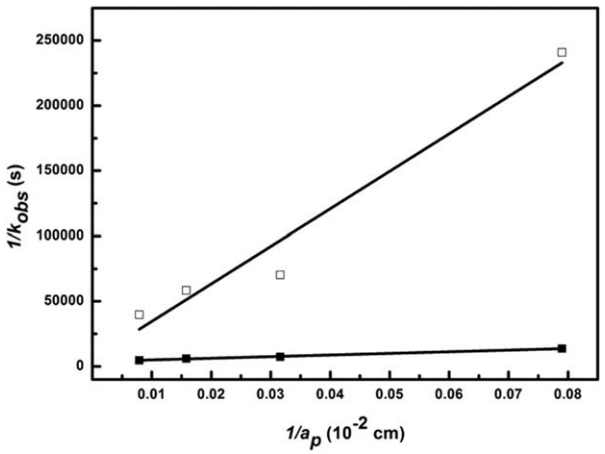

Figure 9. Relationship between $1/a_p$ and $1/k_{obs}$: rate-constant of first step (■) and secondstep (□).

phenol and H_2O_2 were both dropped with a decrease in the loading amount of catalyst. The initial degradation rate of phenol (average within the first 60 s) decreased from 0.49 to 0.11 mM min^{-1} with a decrease in the dosing amount to 10 mg/L. The pH value was slightly changed during the first 900 s and reached to 4.0. This indicated a complex reaction pathway for Fe/SBA-15-MF.

The decomposition of H_2O_2 over metal oxide catalysts is assumed to go through a radical chain mechanism and the redox process. The decomposition process usually followed a first-order rate with respect to H_2O_2 by following a two-step reaction (Figure 8b). The rate-constant (k_{obs}) of each step is summarized in Table 2, which is calculated by Eq. 4

$$r = k_{obs}[H_2O_2] \tag{4}$$

$$\ln\left([H_2O_2]/[H_2O_2]_{t=0}\right) = -k_{obs}t \tag{5}$$

To evaluate the fluid segregation, the extent of interphase transport was investigated by estimating the value of Damkohler number (*Da*) according to Eq. 6

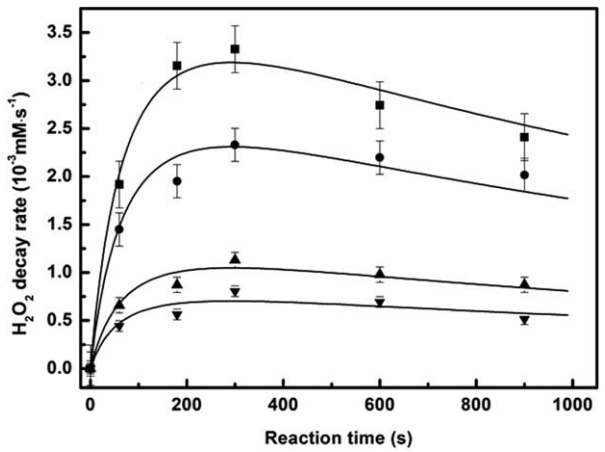

Figure 10. Model verification for the decomposition of H_2O_2 under different loading amount of catalysts:10 mg/L (■); 75 mg/L (•); 100 mg/L (▲); 200 mg/L (▼).

Reaction condition: 313 K, pH = 4.5, $[phenol]_0$ = 1.06 mM, $[H_2O_2]_0$ = 14.71 mM.

$$Da = \frac{k_s[H_2O_2]^{n-1}}{k_c} \tag{6}$$

where k_s refers to the local surface rate-constant with the unit of length per time, k_c is the mass-transport coefficient, which could be estimated to 0.01 cm s^{-1}.*n* represents the reaction order of H_2O_2. At the steady state, we can get the effect of interphase and intraphase transport as the following equation (Eq. 7)

$$r = k_c S_{ex}([H_2O_2] - [H_2O_2]_s) = k_{int} S_{ex}[H_2O_2]_s \eta \tag{7}$$

Here, S_{ex} is the exterior surface of the catalyst, k_{int} is the intrinsic rate-constant (cm s^{-1}), and η is the effectiveness factor. The surface concentration of H_2O_2, $[H_2O_2]_s$, can be estimated by Eq. 8

$$[H_2O_2]_s = \frac{k_c[H_2O_2]}{k_c + k_{int}\eta} \tag{8}$$

Additionally, we define the exterior surface area per reaction unit of the catalyst as the following equation

$$a_p = \frac{S_{ex}}{V_r} \tag{9}$$

Then, we can obtain the expression of reaction rate as followed

$$r = a_p\left(\frac{1}{1/\eta k_{int} + 1/k_c}\right)[H_2O_2] \tag{10}$$

With the combination of Eqs. 3 and 9, we could obtain the surface rate-constant by plotting the $1/k_{obs}$vs. $1/a_p$ (Figure 9).The local surface rate-constants for the first and second step are calculated as 3.49×10^{-5} cm/s and 8.68×10^{-4} cm/s, respectively, on the basis of the slope of curves in Figure 9. The *Da* numbers are 3.49×10^{-3} cm/s and 8.68×10^{-2} cm/s for Fe/SBA-15-MF, implying that the film resistance can be ignored during the whole process. Then the efficient factor, η, for the reaction of first order can be obtained by Eq. 11

$$\eta = \frac{1}{1 + D_a} \tag{11}$$

Thus, η equal to 0.99 and 0.92 for the two steps, corresponding to the intrinsic rate-constant of 3.52×10^{-3} cm/s and 9.43×10^{-2} cm/s, respectively. On the basis of N_2 adsorption–desorption curve, the average pore length is 3.4 nm. Additionally, we can get the Thiele modulus according to the following expression (Eq. 11). Here, the diffusion coefficient is usually $10^{-5}-10^{-6}$ cm^2/s

$$\varphi = L\sqrt{\frac{k_{int}}{D}} \tag{12}$$

Thus, the Thiele modulus is in the range of (6.4–193.8) $\times 10^{-6}$ and (3.3–104.9) $\times 10^{-5}$. On the basis of these results, the surface reaction was obviously dominated by the proceeding of the reaction instead of the interdiffusion or extradiffusion.

Plausible mechanism

The decomposition of H_2O_2 over Fe/SBA-15-MF followed a two-step pattern with respect to H_2O_2 concentration, being different with previous studies.[68,69] Within the van der Waals layers, an electron transfer process became feasible.[35,70,71]

Table 3. Rate Constants of the Elemental Surface Reaction

Unit	k_1	k_{-1}	k_2
$M^{-1}\ s^{-1}$	$(19.52 \pm 0.67) \times 10^{-3}$	$(0.25 \pm 0.05) \times 10^{-3}$	$(1.67 \pm 0.08) \times 10^{2}$

We assume that an active complex was formed immediately when FeOCl interacted with H_2O_2, denoted as FH.

Thus, according to the mechanism described by Eq. 13

$$\mathrm{FeOCl}+\mathrm{H_2O_2} \underset{k-1}{\overset{k1}{\leftrightarrow}} \mathrm{FH} \xrightarrow{k2} \mathrm{OH}\cdot/\mathrm{OOH}\cdot/\mathrm{O_2}+\mathrm{FeOCl} \quad (13)$$

the reaction rate of H_2O_2decomposition can be presented as Eqs. 14–16

$$-\frac{d[\mathrm{H_2O_2}]}{dt}=k_2[\mathrm{FH}] \quad (14)$$

$$-\frac{d[\mathrm{FeOCl}]}{dt}=k_1[\mathrm{FeOCl}][\mathrm{H_2O_2}]-k_{-1}[\mathrm{FH}] \quad (15)$$

$$[\mathrm{FeOCl}]+[\mathrm{FH}]=[\mathrm{FeOCl}]_0 \quad (16)$$

Taking the mass balance of FeOCl on the catalyst into account, the following expression (Eq. 17) can be obtained

$$-\frac{d[\mathrm{FH}]}{dt}=k_1[\mathrm{FeOCl}][\mathrm{H_2O_2}]-k_{-1}[\mathrm{FH}]-k_2[\mathrm{FH}]=0 \quad (17)$$

Assuming the steady state for the yield of the active complex, its concentration can be described by Eq. 18.

$$[\mathrm{FH}]=\frac{[\mathrm{FeOCl}]_0[\mathrm{H_2O_2}]}{\frac{k_{-1}+k_2}{k_1}+[\mathrm{H_2O_2}]} \quad (18)$$

Substitution of Eq. 14 with Eq. 18 obtained Eq. 19 for H_2O_2 decomposition. The expression was an inhibited type of the Langmuir–Hinshelwood equation. The formation of the active complex with a steady state was responsible for the decay of H_2O_2

$$r_{\mathrm{H_2O_2}}=-\frac{d[\mathrm{H_2O_2}]}{dt}=-\frac{k_2[\mathrm{FeOCl}]_0[\mathrm{H_2O_2}]}{\frac{k_{-1}+k_2}{k_1}+[\mathrm{H_2O_2}]} \quad (19)$$

The model calibration was carried out by fitting the experimental data (Figure 8b) into the calculated model, which was also demonstrated (Figure 10). The calculated rate constants were outlined in Table 3. Compared with the subsequent decomposition process, the accumulation of the active complex was relatively slow.

Generally, HO· generated in the Fenton system is considered to be a primary oxidant for the degradation of persistent organic compounds in aqueous solutions.[72] The rate for phenol degradation is greatly dependent on the concentration of HO·. Conversely, HO· scavenging occurs by its interaction with H_2O_2 molecule and other reactive oxidative species (ROS) during the reaction. However, in the solid–liquid reaction systems, HO· is mainly consumed by the quenching effect of the solid surfaces.[73,74] Surprisingly, this study has demonstrated that pure FeOCl shows a superior productivity of HO· compared to the conventional Fenton catalyst. Therefore, it is understandable that the performance for the new advanced oxidation system (FeOCl and H_2O_2) is comparable to that for the conventional Fenton reagent.

The plausible mechanism for the overall reaction was illustrated in Scheme 2. The degradation reaction has been suggested to occur in the water phase near the catalyst surfaces,[75] since HO·, as a short lifetime species (the lifetime of HO· is ~20 ns.), cannot be stabilized in aqueous solutions. HO· is assumed to be released into water immediately once generated. It means the oxidative degradation of organic compounds should follow the similar pathway as identified for the conventional Fenton reaction.[39]

The advantages of FeOCl as a solid Fenton-like catalyst for the production of HO· can be summarized as:

1. Thin water film was proposed to form on the FeOCl surface, which is less affinitive to water. Thus, HO·scavenging is perhaps suppressed by its rapid diffusion into water phase.

2. H_2O_2, as a Lewis base, is much more affinitive to the polarized facet compared to water. The charge transfer occurs between the adsorbed H_2O_2 and Fe atom located at the sublayers. In steady of the intercalation of H_2O_2 into the framework of FeOCl, HO· is generated and diffused into the solution immediately.

3. The lack of the vacancy in FeOCl will lead to a poor scavenging effect comparing to other iron hydroxide or oxides.

Conclusions

Pure and supported FeOCl, as emerging environmental catalysts, were successfully prepared, and its unique structure was thoroughly characterized using XRD, SEM, Raman, UV-vis, and IR spectroscopies. EPR spectra demonstrated the high activity of FeOCl for the production of HO·by the decomposition of H_2O_2. Moreover, different from other solid Fenton-like catalysts, FeOCl exhibited strong capability to resist the interaction with water, thus explaining well that less Fe was leached during the reaction, even in acidic solutions (pH ~ 4.5). The plausible mechanism for H_2O_2 decomposition over solid Fenton-like catalysts was envisaged with the association of the intercalated structure of FeOCl and

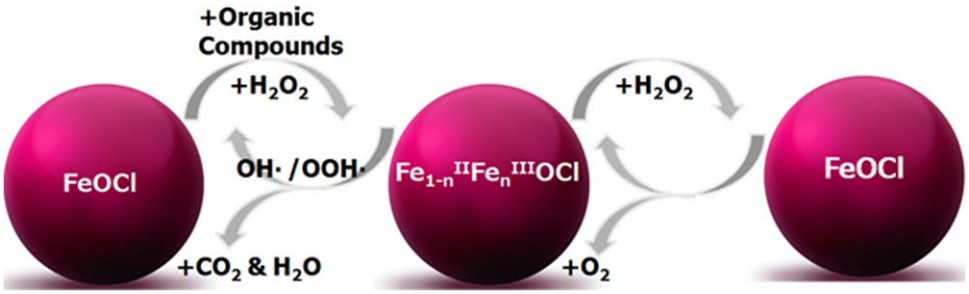

Scheme 2. Plausible mechanism for Fenton-like reaction.

[Color figure can be viewed in the online issue, which is available at wileyonlinelibrary.com.]

kinetic behavior. We believe FeOCl can be a promising alternative for the next generation of solid Fenton-like catalysts; especially, the advanced oxidation reaction over those catalysts will be more practical for the large-scale water treatment.

Acknowledgments

The authors are grateful to the support from the National Science Foundation (21176071, 21106041, 21273070), the Program for New Century Excellent Talents in university (NCET-12-0852), Science and Technology Commission of Shanghai Municipality (11JC1402700, 14230710700), Shanghai Natural Science Foundation (11ZR1408400), Fundamental Research Funds for the Central Universities and the Chinese Education Ministry 111 project (B08021). The authors also thank Dr. Di He from New South Wales University for the informative advise and Mr. Xinchao Xu for the helpful discussion.

Literature Cited

1. Schwarzenbach RP, Escher BI, Fenner K, Hofstetter TB, Johnson CA, von Gunten U, Wehrli B. The challenge of micropollutants in aquatic systems. *Science*. 2006;313(5790):1072–1077.
2. Rokhina EV, Virkutyte J. Environmental application of catalytic processes: heterogeneous liquid phase oxidation of phenol with hydrogen peroxide. *Crit Rev Environ Sci Technol*. 2010;41(2):125–167.
3. Neyens E, Baeyens J. A review of classic Fenton's peroxidation as an advanced oxidation technique. *J Hazard Mater*. 2003;98(1–3):33–50.
4. Mantzavinos D, Kassinos D, Parsons SA. Applications of advanced oxidation processes in wastewater treatment. *Water Res*. 2009; 43(16):3901.
5. Andreozzi R, Caprio V, Insola A, Marotta R. Advanced oxidation processes (AOP) for water purification and recovery. *Catal Today*. 1999;53(1):51–59.
6. Bautista P, Mohedano AF, Casas JA, Zazo JA, Rodriguez JJ. An overview of the application of Fenton oxidation to industrial wastewaters treatment. *J Chem Technol Biotechnol*. 2008;83(10):1323–1338.
7. Hartmann M, Kullmann S, Keller H. Wastewater treatment with heterogeneous Fenton-type catalysts based on porous materials. *J Mater Chem*. 2010;20(41):9002–9017.
8. Dhakshinamoorthy A, Navalon S, Alvaro M, Garcia H. Metal nanoparticles as heterogeneous Fenton catalysts. *ChemSusChem*. 2012; 5(1):46–64.
9. Garrido-Ramírez EG, Theng BKG, Mora ML. Clays and oxide minerals as catalysts and nanocatalysts in Fenton-like reactions—a review. *Appl Clay Sci*. 2010;47(3–4):182–192.
10. Pham AN, Xing G, Miller CJ, Waite TD. Fenton-like copper redox chemistry revisited: hydrogen peroxide and superoxide mediation of copper-catalyzed oxidant production. *J Catal*. 2013;301:54–64.
11. Xiao F-S, Sun J, Meng X, et al. Synthesis and structure of copper hydroxyphosphate and its high catalytic activity in hydroxylation of phenol by H_2O_2. *J Catal*. 2001;199(2):273–281.
12. Subbaramaiah V, Srivastava VC, Mall ID. Catalytic activity of Cu/SBA-15 for peroxidation of pyridine bearing wastewater at atmospheric condition. *AIChE J*. 2013;59(7):2577–2586.
13. Han Y-F, Chen F, Ramesh K, Zhong Z, Widjaja E, Chen L. Preparation of nanosized Mn3O4/SBA-15 catalyst for complete oxidation of low concentration EtOH in aqueous solution with H2O2. *Appl Catal B: Environ*. 2007;76(3–4):227–234.
14. Sriskandakumar T, Opembe N, Chen C-H, Morey A, King'ondu C, Suib SL. Green decomposition of organic dyes using octahedral molecular sieve manganese oxide catalysts. *J Phys Chem A*. 2009; 113(8):1523–1530.
15. Valdés-Solís T, Valle-Vigón P, Sevilla M, Fuertes AB. Encapsulation of nanosized catalysts in the hollow core of a mesoporous carbon capsule. *J Catal*. 2007;251(1):239–243.
16. Heckert EG, Seal S, Self WT. Fenton-like reaction catalyzed by the rare earth inner transition metal cerium. *Environ Sci Technol*. 2008; 42(13):5014–5019.
17. Han Y-F, Phonthammachai N, Ramesh K, Zhong Z, White T. Removing organic compounds from aqueous medium via wet peroxidation by gold catalysts. *Environ Sci Technol*. 2007;42(3):908–912.
18. Yang X, Tian P-F, Zhang C, Deng Y-q, Xu J, Gong J, Han Y-F. Au/carbon as Fenton-like catalysts for the oxidative degradation of bisphenol A. *Appl Catal B: Environ*. 2013;134–135:145–152.
19. Navalon S, de Miguel M, Martin R, Alvaro M, Garcia H. Enhancement of the catalytic activity of supported gold nanoparticles for the Fenton reaction by light. *J Am Chem Soc*. 2011;133(7):2218–2226.
20. Prucek R, Hermanek M, Zboril R. An effect of iron(III) oxides crystallinity on their catalytic efficiency and applicability in phenol degradation—a competition between homogeneous and heterogeneous catalysis. *Appl Catal A: Gen*. 2009;366(2):325–332.
21. Guimarães IR, Oliveira LCA, Queiroz PF, Ramalho TC, Pereira M, Fabris JD, Ardisson JD. Modified goethites as catalyst for oxidation of quinoline: evidence of heterogeneous Fenton process. *Appl Catal A: Gen*. 2008;347(1):89–93.
22. Kwan WP, Voelker BM. Decomposition of hydrogen peroxide and organic compounds in the presence of dissolved iron and ferrihydrite. *Environ Sci Technol*. 2002;36(7):1467–1476.
23. Rusevova K, Kopinke F-D, Georgi A. Nano-sized magnetic iron oxides as catalysts for heterogeneous Fenton-like reactions—influence of Fe(II)/Fe(III) ratio on catalytic performance. *J Hazard Mater*. 2012;241–242:433–440.
24. Rey A, Faraldos M, Bahamonde A, Casas JA, Zazo JA, Rodríguez JJ. Role of the activated carbon surface on catalytic wet peroxide oxidation. *Ind Eng Chem Res*. 2008;47(21):8166–8174.
25. Duarte F, Maldonado-Hódar FJ, Madeira LM. Influence of the particle size of activated carbons on their performance as Fe supports for developing Fenton-like catalysts. *Ind Eng Chem Res*. 2012;51(27): 9218–9226.
26. Fernandez J, Bandara J, Kiwi J, Lopez A, Albers P. Efficient photoassisted Fenton catalysis mediated by Fe ions on Nafion membranes active in the abatement of non-biodegradable azo-dye. *Chem Commun*. 1998;14:1493–1494.
27. Parra S, Henao L, Mielczarski E, Mielczarski J, Albers P, Suvorova E, Guindet J, Kiwi J. Synthesis, testing, and characterization of a novel nafion membrane with superior performance in photoassisted immobilized fenton catalysis. *Langmuir*. 2004;20(13):5621–5629.
28. Pham AL, Lee C, Doyle FM, Sedlak DL. A silica-supported iron oxide catalyst capable of activating hydrogen peroxide at neutral pH values. *Environ Sci Technol*. 2009;43(23):8930–8935.
29. Martínez F, Calleja G, Melero JA, Molina R. Iron species incorporated over different silica supports for the heterogeneous photo-Fenton oxidation of phenol. *Appl Catal B: Environ*. 2007;70:452–460.
30. Feng J, Hu X, Yue PL. Novel Bentonite clay-based Fe-nanocomposite as a heterogeneous catalyst for photo-Fenton discoloration and mineralization of orange II. *Environ Sci Technol*. 2003;38(1):269–275.
31. Kasiri MB, Aleboyeh H, Aleboyeh A. Degradation of acid blue 74 using Fe-ZSM5 zeolite as a heterogeneous photo-Fenton catalyst. *Appl Catal B: Environ*. 2008;84(1-2):9–15.
32. Kasiri MB, Aleboyeh H, Aleboyeh A. Modeling and optimization of heterogeneous photo-Fenton process with response surface methodology and artificial neural networks. *Environ Sci Technol*. 2008; 42(21):7970–7975.
33. Parra S, Guasaquillo I, Enea O, Mielczarski E, Mielczarki J, Albers P, Kiwi-Minsker L, Kiwi J. Abatement of an azo dye on structured C-Nafion/Fe-Ion surfaces by photo-Fenton reactions leading to carboxylate intermediates with a remarkable biodegradability increase of the treated solution. *J Phys Chem B*. 2003;107(29):7026–7035.
34. Kanamaru F, Shimada M, Koizumi M, Takano M, Takada T. Mössbauer effect of FeOCl-pyridine complex. *J Solid State Chem*. 1973;7(3):297–299.
35. Jarrige I, Cai YQ, Shieh SR, et al. Charge transfer in FeOCl intercalation compounds and its pressure dependence: an x-ray spectroscopic study. *Phys Rev B*. 2010;82(16):165121.
36. Yang X-j, Xu X-m, Xu J, Han Y-f. Iron oxychloride (FeOCl): an efficient Fenton-like catalyst for producing hydroxyl radicals in degradation of organic contaminants. *J Am Chem Soc*. 2013;135(43): 16058–16061.
37. Kanungo SB, Mishra SK. Thermal dehydration and decomposition of $FeCl_3 \cdot xH_2O$. *J Therm Anal*. 1996;46(5):1487–1500.
38. Kanungo SB, Mishra SK. Kinetics of thermal dehydration and decomposition of Fe(III) chloride hydrate ($FeCl_3 \cdot xH_2O$). *J Therm Anal*. 1997;48(2):385–401.

39. Zazo JA, Casas JA, Mohedano AF, Gilarranz MA, Rodríguez JJ. Chemical pathway and kinetics of phenol oxidation by Fenton's reagent. *Environ Sci Technol*. 2005;39(23):9295–9302.
40. Zhao D, Huo Q, Feng J, Chmelka BF, Stucky GD. Nonionic triblock and star diblock copolymer and oligomeric surfactant syntheses of highly ordered, hydrothermally stable, mesoporous silica structures. *J Am Chem Soc*. 1998;120:6024–6036.
41. Eggenhuisen TM, den Breejen JP, Verdoes D, de Jongh PE, de Jong KP. Fundamentals of melt infiltration for the preparation of supported metal catalysts. The case of Co/SiO2 for Fischer−Tropsch synthesis. *J Am Chem Soc*. 2010;132(51):18318–18325.
42. Lázár K, Calleja G, Melero JA, Martinez F, Molina R. Influence of synthesis routes on the state of Fe-species in SBA-15 mesoporous materials. In: van Steen E, Callanan LH, Claeys M, editors. *Studies in Surface Science and Catalysis*. Vol. 154, Part A: Elsevier, 2004: 805–812.
43. Lim H, Lee J, Jin S, Kim J, Yoon J, Hyeon T. Highly active heterogeneous Fenton catalyst using iron oxide nanoparticles immobilized in alumina coated mesoporous silica. *Chem Commun*. 2006;4:463–465.
44. Herber RH, Maeda Y. Synthesis, hyperfine interactions, and lattice dynamics of the intercalation compounds FeOCl [(CH3O)3P]1/6 and FeOCl [(CH3CH2)3P]1/6. *Inorg Chem*. 1980;19(11):3411–3418.
45. Kuzmic P. Program DYNAFIT for the analysis of enzyme kinetic data: application to HIV proteinase. *Anal Biochem*. 1996;237(2): 260–273.
46. Cohen IR, Purcell TC, Altshuller AP. Analysis of the oxidant in photooxidation reactions. *Environ Sci Technol*. 1967;1(3):247–252.
47. de Faria DLA, Venâncio Silva S, de Oliveira MT. Raman microspectroscopy of some iron oxides and oxyhydroxides. *J Raman Spectrosc*. 1997;28(11):873–878.
48. Cesar I, Sivula K, Kay A, Zboril R, Graetzel M. Influence of feature size, film thickness, and silicon doping on the performance of nanostructured hematite photoanodes for solar water splitting. *J Phys Chem C*. 2009;113(2):772–782.
49. Jubb AM, Allen HC. Vibrational spectroscopic characterization of hematite, maghemite, and magnetite thin films produced by vapor deposition. *ACS Appl Mater Interfaces*. 2010;2(10):2804–2812.
50. Avery JS, Burbridge CD, Goodgame DML. Raman spectra of tetrahalo-anions of Fe III, Mn II, Fe II, Cu IIand Zn II. *Spectrochim Acta*. 1968;24(11):1721–1726.
51. Oh S, Cook DC, Townsend HE. Characterization of iron oxides commonly formed as corrosion products on steel. *Hyperfine Interact*. 1998;112(1):59–66.
52. Thibeau RJ, Brown CW, Heidersbach RH. Raman spectra of possible corrosion products of iron. *Appl Spectrosc*. 1978;32(6):532–535.
53. Thierry D, Persson D, Leygraf C, Boucherit N, Hugot-le Goff A. Raman spectroscopy and XPS investigations of anodic corrosion films formed on FeMo alloys in alkaline solutions. *Corros Sci*. 1991; 32(3):273–284.
54. Cornell RM, Schwertmann U. *The Iron Oxide*. Weinheim: WILEY-VCH Verlag GmbH &Co., 2003.
55. Chernyshova IV, Hochella MF Jr, Madden AS. Size-dependent structural transformations of hematite nanoparticles. 1. Phase transition. *Phys Chem Chem Phys*. 2007;9(14):1736–1750.
56. Pradhan GK, Parida KM. Fabrication, growth mechanism, and characterization of α-Fe2O3 nanorods. *ACS Appl Mater Interfaces*. 2011; 3(2):317–323.
57. Ruan HD, Frost RL, Kloprogge JT. The behavior of hydroxyl units of synthetic goethite and its dehydroxylated product hematite. *Spectrochim Acta Part A: Mol Biomol Spectrosc*. 2001;57(13):2575–2586.
58. Choy J-H, Kang J-W, Kwon Y-U. Formation of layered compounds of $FeO(OCH_3)_{0.7}Cl_{0.3}$ and $FeO(OC_2H_5)_{0.3}Cl_{0.7}$ by topochemical reaction. *Bull Korean Chem Soc*. 1983;6(4):251–253.
59. Pérez-Ramírez J, Santhosh Kumar M, Brückner A. Reduction of N2O with CO over FeMFI zeolites: influence of the preparation method on the iron species and catalytic behavior. *J Catal*. 2004; 223(1):13–27.
60. Kumar MS, Schwidder M, Grünert W, Brückner A. On the nature of different iron sites and their catalytic role in Fe-ZSM-5 $DeNO_x$ catalysts: new insights by a combined EPR and UV/VIS spectroscopic approach. *J Catal*. 2004;227(2):384–397.
61. Li Y, Feng Z, Xin H, Fan F, Zhang J, Magusin PCMM, Hensen EJM, van Santen RA, Yang Q, Li C. Effect of aluminum on the nature of the iron species in Fe-SBA-15. *J Phys Chem B*. 2006; 110(51):26114–26121.
62. Sherman DM, Waite TD. Electronic spectra of Fe (super 3+) oxides and oxide hydroxides in the near IR to near UV. *Am Mineral*. 1985; 70(11–12):1262–1269.
63. Zazo J, Casas J, Mohedano A, Rodriguez J. Semicontinuous Fenton oxidation of phenol in aqueous solution. A kinetic study. *Water Res*. 2009;43(16):4063–4069.
64. Quintanilla A, García-Rodríguez S, Domínguez CM, Blasco S, Casas JA, Rodriguez JJ. Supported gold nanoparticle catalysts for wet peroxide oxidation. *Appl Catal B: Environ*. 2012;111–112:81–89.
65. Esplugas S, Giménez J, Contreras S, Pascual E, Rodríguez M. Comparison of different advanced oxidation processes for phenol degradation. *Water Res*. 2002;36(4):1034–1042.
66. Han SK, Hwang T-M, Yoon Y, Kang J-W. Evidence of singlet oxygen and hydroxyl radical formation in aqueous goethite suspension using spin-trapping electron paramagnetic resonance (EPR). *Chemosphere*. 2011;84(8):1095–1101.
67. Levenspiel O. *Chemical Reaction Engineering*. Vol 2. New York: Wiley, 1972.
68. Lin S-S, Gurol MD. Catalytic decomposition of hydrogen peroxide on iron oxide: kinetics, mechanism, and implications. *Environ Sci Technol*. 1998;32(10):1417–1423.
69. Pham AL-T, Doyle FM, Sedlak DL. Kinetics and efficiency of H_2O_2 activation by iron-containing minerals and aquifer materials. *Water Res*. 2012;46(19):6454–6462.
70. Wu CG, DeGroot DC, Marcy HO, Schindler JL, Kannewurf CR, Bakas T, Papaefthymiou V, Hirpo W, Yesinowski JP. Reaction of aniline with FeOCl. Formation and ordering of conducting polyaniline in a crystalline layered host. *J Am Chem Soc*. 1995;117(36): 9229–9242.
71. Kauzlarich SM, Ellena JF, Stupik PD, Rieff WM, Averill BA. Spectroscopic and magnetic properties of FeOCl intercalated with organosulfur electron donors. *J Am Chem Soc*. 1987;109(15):4561–4570.
72. Pignatello JJ, Oliveros E, MacKay A. Advanced oxidation processes for organic contaminant destruction based on the Fenton reaction and related chemistry. *Crit Rev Environ Sci Technol*. 2006;36(1):1–84.
73. Xue Y, Luan Q, Yang D, Yao X, Zhou K. Direct evidence for hydroxyl radical scavenging activity of cerium oxide nanoparticles. *J Phys Chem C*. 2011;115(11):4433–4438.
74. Fenoglio I, Tomatis M, Lison D, Muller J, Fonseca A, Nagy JB, Fubini B. Reactivity of carbon nanotubes: free radical generation or scavenging activity? *Free Radical Biol Med*. 2006;40(7):1227–1233.
75. Kwan WP. *Decomposition of Hydrogen Peroxide and Orangic Compounds in the Presence of Iron and Iron Oxides*. Massachusetts: Department of Civil and Environmental Engineering Massachusetts Institute of Technology, 2003.

Manuscript received Mar. 31, 2014, and revision received Sep. 2, 2014.